Spatial-Spectral Hyperspectral Endmember Extraction Using a Spatial Energy Prior Constrained Maximum Simplex Volume Approach

Xiangfei Shen, Wenxing Bao, and Kewen Qu

***Abstract*—Endmember extraction algorithms (EEAs) are among the most commonly discussed types of hyperspectral image processing in the past three decades. This article proposes a spatial energy prior constrained maximum simplex volume (SENMAV) approach for spatial-spectral endmember extraction of hyperspectral images. SENMAV investigates the spatial information from the perspective of the spatial energy prior of a Markov random field (MRF), which is used as a regularization term of the traditional maximum volume simplex model to simultaneously constrain the selection of the endmembers in both the spatial and spectral viewpoints. This article sheds new light on spatial-spectral-based EEAs, as SENMAV well balances the tradeoff between endmember extraction accuracy and spatial attribute requirements of endmembers. Based on the spectral angle distance and root-mean-square error, experimental results on both synthetic and real hyperspectral datasets indicate that the proposed approach significantly improves the endmember extraction performance over current state-of-the-art spatial-spectral-based EEAs.**

***Index Terms*—Endmember extraction algorithm (EEA), hyperspectral imagery, maximum simplex volume, spatial energy prior, spatial spectral.**

I. Introduction

IF THE spatial resolution of a hyperspectral sensor is coarser than the scale of spatial heterogeneity of the ground surface, a mixture of disparate substances is inevitably contained in a pixel [1], [2]. A pixel that mixes more than one distinct substance is called a *mixed pixel* in a hyperspectral image (HSI). The process that decomposes the mixed pixels into a set of constituent spectra, or *endmembers*, and their corresponding proportions, or *abundances*, is called hyperspectral unmixing (HU) [3], [4].

Manuscript received November 28, 2019; revised January 27, 2020 and February 21, 2020; accepted March 11, 2020. Date of publication April 2, 2020; date of current version April 20, 2020. This work was supported in part by the National Natural Science Foundation of China under Project No. 61461003 and in part by the Innovation Projects for Graduate Students of North Minzu University (Project No. YCX19057). *(Corresponding author: Wenxing Bao.)*

Xiangfei Shen is with the School of Computer Science and Engineering, North Minzu University, Yinchuan 750021, China (e-mail: 20177197@stu.nmu.edu.cn).

Wenxing Bao and Kewen Qu are with the School of Computer and Information, Hefei University of Technology, Hefei 230009, China, and also with the School of Computer Science and Engineering, North Minzu University, Yinchuan 750021, China (e-mail: bwx71@163.com; kewen.qu@aliyun.com).

Digital Object Identifier 10.1109/JSTARS.2020.2981402

According to the illumination type, HU algorithms are divided into two types: the nonlinear mixing model (NLMM), which assumes that the light follows a multiple scattering phenomenon; and the linear mixing model (LMM), which assumes that the light is a linear combination of different materials. Among them, NLMM assumption-based HU algorithms face more challenges, as they must establish a more complex physical model to simulate potential light scattering types. A new line of research into NLMM problems is based on deep learning methods such as neural networks. Compared with the classic bilinear or intimate mixing models in the NLMM field, proposed neural network-based HU algorithms such as EndNet [5], pixel-based CNN [6], and cube-based CNN [6] show more promising performance. However, they require appropriate computation equipment or parameters to maintain their performance, which is not always guaranteed and efficient. LMM assumption-based algorithms have more clear conceptual meaning to easily capture endmember extraction and abundance estimation, owing to multiple priors of data matrices such as sparse [7], [8], low-rank [9], and geometric [10] properties, which have attracted considerable attention [2], [3].

Based on the LMM assumption-based algorithms, the processes of endmember determination and abundance estimation are normally seen as two separate aspects. However, the determination of endmembers has received more attention than abundance estimation, since good representations of surface components are necessary for accurate unmixing [11]. The last three decades have witnessed huge growth in endmember extraction algorithms (EEAs). These can be categorized as pure pixel assumption-based, nonpure pixel assumption-based, and statistical-based [3].

Pure pixel assumption-based EEAs assume that there exists at least one pure pixel per endmember extracted within the HSI. These can be further divided into three types. First, subspace projection-based EEAs determine endmembers by considering their extreme projections on a subspace. These include the pixel purity index (PPI) [12], orthogonal subspace projection [13], and vertex component analysis (VCA) [14]. Second, maximum simplex volume-based EEAs identify endmembers by defining a maximum simplex volume under the conditions of a dimensionality-reduced HSI. These include N-FINDR [15],

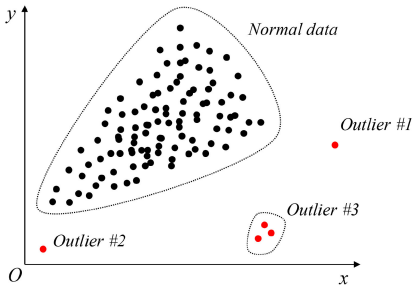

(a)

Fig. 1. Example of normal data and outliers in a two-dimensional dataset. Points sufficiently far from the normal data distribution include outliers #1, #2, and #3.

simplex growing algorithm (SGA) [16], and successive volume maximization [17]. Third, least-squares-based EEAs select the pixel that can minimize the unmixing errors. These include iterative error analysis [18] and the unsupervised fully constrained least-squares method [19].

Nonpure pixel assumption-based EEAs assume not that pure pixels exist in the dataset, but that there exist at least $p-1$ spectra on each facet to specify a minimum simplex volume. These include minimum volume transform (MVT) [20], minimum volume enclosing simplex [21], the simplex identification via variable splitting and augmented Lagrangian approach [22], and minimum volume simplex analysis (MVSA) [23].

Statistical-based algorithms are indispensable when the spectral vectors are highly mixed, resulting in simplex being unavailable for endmember extraction. These include dependent component analysis [24], iterated constrained endmembers [25], and minimum volume constrained nonnegative matrix factorization [10].

Most of the abovementioned EEAs consider spectral information for endmember extraction in a single perspective, while ignoring the intrinsic attribute of spatial contextual information. In this regard, these EEAs are susceptible to outliers, which are inevitable in HSIs. In general, outliers are special patterns in data without a well-defined notion of normal behavior, and their signatures are spectrally distinct from their surroundings or background representation [26], [27]. They are potentially generated during detector failure, data transfer, and improper data correction [28]. Outliers are more likely to be selected as endmembers by most spectral-based EEAs because they deeply deviate from the background data, and they may force a vertex of the simplex to reside at a point beyond the nominal position of the endmember in order to enclose every point [4]. An example of normal data and outliers in a two-dimensional dataset is displayed in Fig. 1. In this article, we refer to such an outlier as $endmemberlike$. However, the literature rarely discusses the relationship between true endmembers and the endmemberlike.

The HSI is conceptually a two-dimensional pictorial representation of the ground surface, with both spatial and spectral attributes [1]. There has been great interest in spatial-spectral-based EEAs and spatial-spectral-based preprocessing algorithms (PPAs) in the past two decades. Spatial-spectral-based EEAs rely heavily on a combination of spectral features and spatial contextual information of the hyperspectral data for the purpose of endmember extraction. Typical techniques include automated morphological endmember extraction (AMEE) [29], spatial spectral information-based endmember extraction (SSEE) [30], the hybrid automatic endmember extraction algorithm [31], the spatial purity-based endmember extraction algorithm (SPEE) [32], and spatial-spectral information-based endmember bundle extraction (SSEBE) [27]. However, spatial-spectral-based EEAs generally suffer from a computational burden since many dot-product or graph-based methods are involved, and manually tuned parameters require optimized endmember extraction. More importantly, few regard the convexity of the data, which accounts for high-performance endmember extraction, which most spectral-based EEAs consider. Spatial-spectral-based PPAs utilize both spatial and spectral information with the specific intent to offer a few high-quality candidates for fast endmember extraction [33]. Representative algorithms include spatial preprocessing (SPP) [34], spatial-spectral preprocessing [35], and regional-clustering-based spatial preprocessing [36]. Unlike EEAs, spatial-spectral-based PPAs are independently executed modules that provide a few high-quality endmember candidates prior to the endmember extraction search process.

Based on Tobler's first law of geography, "Everything is related to everything else, but near things are more related than distant things" [37], the endmembers extracted within the HSI also should be spatially and spectrally close to its neighborhoods. More importantly, a basic assumption of the HSI is that two neighboring pixels more likely belong to the same class, indicating that their spectral signatures should be highly similar. This assumption is also generally derived from the Markov random field (MRF), which is the classical model to exploit neighborhood dependence between pixels. Several studies [38]–[42], have been carried out on MRF; however, much of the emphasis has been on enhancing spatial dependence or smoothing labels in hyperspectral classification or segmentation fields.

In this article, we develop a spatial energy prior constrained maximum simplex volume (SENMAV) approach for spatial-spectral-oriented hyperspectral endmember extraction. Specifically, the proposed SENMAV method analyzes the spatial energy prior of hyperspectral data, and this is utilized as a regularization term coupled with a maximum simplex volume model to simultaneously constrain the selection of endmembers in both spatial and spectral perspectives. We make the following three primary contributions.

1) A new spatial-spectral-based EEA is proposed by incorporating a spatial energy prior into the maximum simplex volume.
2) The proposed algorithm well balances the tradeoff between endmember extraction accuracy and spatial attribute requirements of endmembers.
3) The proposed algorithm avoids the traps of spectral-based EEA sensitivity to outliers and inefficient endmember extraction performance of spatial-spectral-based EEAs.

Several experiments conducted on both synthetic and real hyperspectral datasets indicate that the proposed approach significantly improves upon current state-of-the-art EEAs.

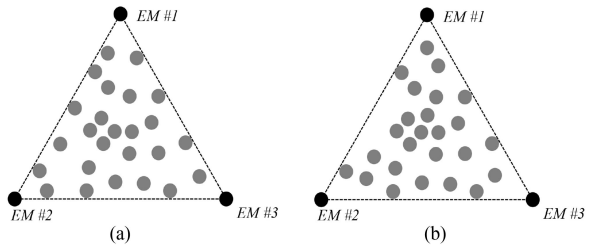

Fig. 2. Two well-known paradigms in the spectral-based endmember extraction fields. (a) First assumes that there exists at least one pure pixel per endmember in each vertex. (b) Second assumes that there exist at least $p-1$ spectra on each facet.

The rest of this article is organized as follows. Section II briefly discusses the background, including work on spectral-based and spatial-spectral-based EEA, and reviews the theory of LMM and MRF. Section III describes the proposed algorithm. Experimental results and discussion of this method are presented in Sections IV and V, respectively. Section VI concludes this article with some remarks.

II. Background

A. Related Work

1) Spectral-Based EEA: In the past several decades, spectral-based EEAs have come under the spotlight in HU owing to their clear conceptual meaning. Specifically, under the LMM assumption, endmember extraction can be seen as a process of fitting a simplex around the convex hull of the data [43]. Two well-known paradigms in the spectral-based endmember extraction fields are displayed in Fig. 2.

Preliminary work in this field focused primarily on the PPI [12], in which entire spectral vectors are projected onto a large number of randomly generated $skewers$, and then the number of times spectral vectors are found to have extreme projection values are used to determine desired endmembers. However, it may be difficult for the PPI to identify a final list of endmembers; hence, it is generally used for preprocessing to obtain a set of endmember candidates. Unlike PPI, VCA [14] sequentially selects endmembers by projecting all the spectral vectors onto an orthogonal subspace spanned by the already determined endmembers. This is based on two important facts: the endmembers are the vertices of a simplex; and the affine transformation of a simplex is also a simplex.

N-FINDR [15] is based on the fact that endmembers comprise a set of spectral vectors that can define a maximum volume larger than any other volume formed by interior pixels within the simplex. SGA [16] finds a desired $(p-1)$-dimensional simplex with the largest volume by gradually growing simplexes, vertex by vertex. Similarly, as an extension of N-FINDR, AVMAX [17] attempts to maximize the simplex volume by a one-at-a-time pixel search.

When no pure pixels exist in the scene, many EEAs emphasize the minimization of the simplex volume defined by the column of the endmember matrix. The initial work in this area was the MVT, proposed by Craig [20], which begins with a simplex of large volume and then literally moves the faces of the simplex in toward the data cloud. MVSA [23] fits a minimum-volume simplex to the hyperspectral data by constraining the abundance fractions to belong to the probability simplex.

Unfortunately, the abovementioned spectral-based EEAs fail to consider the spatial information of the endmember lying in the HSI. Recently, we proposed a new spatially weighted simplex strategy (SWSS) [33] for hyperspectral endmember extraction, which first generates the spatial weight scalar of each pixel by determining its corresponding spatial neighborhood correlations for weighting itself within the simplex framework to regularize the selection of the endmembers. However, SWSS can only be coupled with pure pixel assumption-based EEAs.

2) Spatial-Spectral-Based EEA: Considering that most EEAs have been designed from a spectroscopic viewpoint, the spatial attributes of pixels lying in the HSI have tended to be ignored. Therefore, most spatial-spectral-based EEAs assume that endmembers are more likely to be found in spatially homogeneous areas.

The first systematic study on spatial-spectral-based EEAs was carried out in 2002 by Plaza *et al.* [29]. The proposed AMEE is based on mathematical morphology operators, i.e., erosion and dilation. The erosion operation selects the most highly mixed pixel, while dilation determines the purest pixel. A morphological eccentricity index is defined to select endmembers by an iterative process at a dynamically spatial sliding kernel window. SSEE [30] first acquires the endmember candidate set after projecting all the subset data onto eigenvectors decomposed by SVD techniques. Endmember candidates are then reordered based on spectral similarity. Finally, the endmembers are generated by spatial averaging of the endmember candidates and the spatially and spectrally close updated candidate pixels. SPEE [32] first investigates several intensity- and feature-level spatial purity measurements to generate initial endmember candidates. Second, a pure spatial neighborhood is voted as an endmember candidate to alleviate spectral variability. A graph theory-based spatial refinement algorithm is then used to refine endmember candidates in a spatial context. Endmember candidates are further refined using a clustering method. A recent development in this area is SSEBE [27], which performs the following steps.

1) PPI preprocessing generates a set of endmember candidates.
2) Each endmember candidate is used to calculate the homogeneity index (HI) between its neighborhoods and itself.
3) An adaptive threshold of HI is fixed for choosing pure pixels in each block.
4) The clustering method is utilized to group the endmember candidates.

The abovementioned methods include parameters demanding a tuning process to optimize endmember extraction in accordance with different dataset scenarios or algorithmic requirements, and the computation is expensive.

B. LMM

Based on LMM, a measured hyperspectral imagery (HSI) $\mathbf{Y} = [\boldsymbol{y_1}, \boldsymbol{y_2}, \ldots, \boldsymbol{y_n}]_{B\times n}$ with B bands and n total pixels can

be formulated as

$$\mathbf{Y} = \mathbf{MA} + \boldsymbol{\omega} \tag{1}$$

where $\mathbf{M} \in \mathbb{R}^{B\times p}$ is the endmember matrix, $\mathbf{A} \in \mathbb{R}^{p\times n}$ is the abundance fraction matrix, and $\boldsymbol{\omega} \in \mathbb{R}^{B\times n}$ accounts for the additive noise matrix. Also, p is the number of endmembers, which can be estimated by classic techniques such as virtual dimensionality [44].

C. Markov Random Field (MRF)

In the image processing field, MRF is a classic method, which is used to exploit the spatial information of neighbor pixels. The spatial information is based on the assumption that neighboring pixels more likely belong to the same class. The class of a pixel $\boldsymbol{y_i}$ is determined by a class label $\theta_{\boldsymbol{y_i}}$, which is characterized as a discrete random variable derived from the class values set $\boldsymbol{\mathcal{L}} = \{1, 2, \ldots, l\}$. The label set $\boldsymbol{\theta} = \{\theta_{\boldsymbol{y_i}}, \boldsymbol{y_i} \in \mathbf{Y}\}$ is a random field, where $\theta_{\boldsymbol{y_i}} \in \boldsymbol{\mathcal{L}}$. According to the Hammersly–Clifford theorem [45], the spatial prior $P(\boldsymbol{\theta} = \theta_{\boldsymbol{y_i}})$ follows a Gibbs distribution defined as

$$P\left(\boldsymbol{\theta} = \theta_{\boldsymbol{y_i}}\right) = \frac{1}{Z}\exp\left(-U\left(\theta_{\boldsymbol{y_i}}\right)\right) \tag{2}$$

where $Z = \sum_{\theta_{\boldsymbol{y_i}}\in\boldsymbol{\mathcal{L}}} \exp^{-U(\theta_{\boldsymbol{y_i}})}$ is a *partition function*. $U(\theta_{\boldsymbol{y_i}}) = \sum_{c\in C} V_c(\theta_{\boldsymbol{y_i}})$ is an *energy function*, where $V_c(\cdot)$ is the *clique potential function* related to clique c that belongs to C, which is a set of a determined order, e.g., first, second, and high order. To characterize the clique potential function for each clique c, the well-known Potts Markov model [46] is generally used, and this is given by

$$V_c = \delta\left(\theta_{\boldsymbol{y_i}}, \theta_{\boldsymbol{y_j}}\right) = \begin{cases} 1 \text{ if } \theta_{\boldsymbol{y_i}} \neq \theta_{\boldsymbol{y_j}} \\ 0 \text{ otherwise.} \end{cases} \tag{3}$$

According to (2) and (3), the spatial prior can be reformulated as

$$P\left(\boldsymbol{\theta} = \theta_{\boldsymbol{y_i}}\right) = \frac{1}{Z}\exp\left(-\sum_{\{\boldsymbol{y_i},\boldsymbol{y_j}\}\in C}\delta\left(\theta_{\boldsymbol{y_i}}, \theta_{\boldsymbol{y_j}}\right)\right). \tag{4}$$

In the Bayesian framework, the image classification problem can be expressed as the investigation of an optimal labeling $\hat{\boldsymbol{\theta}}$ that maximizes the posterior probability $P(\boldsymbol{\theta}|\mathbf{Y})$, i.e.,

$$\hat{\boldsymbol{\theta}} = \arg\max_{\boldsymbol{\theta}} P\left(\boldsymbol{\theta}|\mathbf{Y}\right) = \arg\max_{\boldsymbol{\theta}} P\left(\mathbf{Y}|\boldsymbol{\theta}\right) P\left(\boldsymbol{\theta}\right). \tag{5}$$

A high-order neighborhood system normally has high computational complexity; hence, the first and second order are two widely used neighborhood systems (see Fig. 3).

III. Spatial Energy Prior Constrained Maximum Simplex Volume

A. Spatial Energy Prior

MRF is based on the understandable assumption that two neighboring pixels more likely belong to the same class. However, the most important issue of MRF is to construct an initial label map. We use the well-known k-means clustering technique to allocate initial labels for each spectral vector. Let

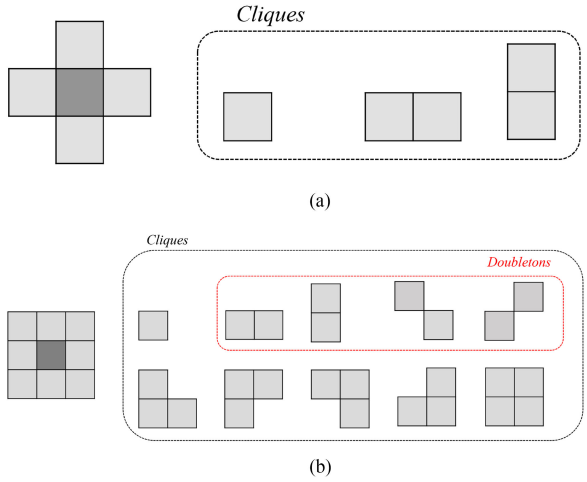

Fig. 3. Visual description of different order neighborhood systems with their corresponding cliques. (a) First-order neighborhood system with corresponding cliques. (b) Second-order neighborhood system with corresponding cliques.

$\hat{\mathbf{Y}} = [\hat{\boldsymbol{y}}_{\mathbf{1}}, \hat{\boldsymbol{y}}_{\mathbf{2}}, \ldots, \hat{\boldsymbol{y}}_{\boldsymbol{n}}]_{(p-1)\times n}$ be a low-dimension HSI, which is reduced by principal component analysis (PCA) [47], with $p-1$ bands and n total pixels. $l \in [p, 2p]$ denotes the maximum potential labels. It is noteworthy that the reason why l is determined in the interval of $[p, 2p]$ lies in the following important points.

1) The number of endmembers is difficult to precisely estimate, especially for large-scale or highly mixed real hyperspectral datasets, owing to the insufficient priors of land cover, and thus, l should be at least greater than p.
2) If l is too large, e.g., $l > 2p$, the computational cost of k-means may increase as well, since the computational complexity of k-means is nlt, where n, l, and t are the data scale, number of preset clusters, and iteration times, respectively.
3) The k-means algorithm is used to assign initial labels for each pixel, and is utilized to calculate the spatial energy prior for the image.

If l is smaller than p, a few minerals may be mistakenly assigned true labels. However, if l is too large, the spatial energy prior of the local area will be low, since such an area is excessively allocated different and wrong labels. The process of determining the initial label map and corresponding centroids is defined as follows:

$$[\boldsymbol{\theta}, \boldsymbol{\Psi}] = \boldsymbol{kmeans}\left(\hat{\mathbf{Y}}, l, t\right) \tag{6}$$

where $\boldsymbol{\theta}$ denotes the initial label map composed of multiple classes varying from 1 to l, $\boldsymbol{\Psi}$ is the centroid matrix associated with the initial label map, and t is the iteration time.

Based on (4) and the initial label map, we redefine the spatial energy prior of a specified pixel, e.g., $\boldsymbol{y_i}$, as follows:

$$\phi_{\text{spatial}}\left(\boldsymbol{y_i}\right) = \exp\left(-\sum_{\{\boldsymbol{y_i},\boldsymbol{y_j}\}\in C}\delta\left(\theta_{\boldsymbol{y_i}}, \theta_{\boldsymbol{y_j}}\right)\right) \tag{7}$$

where C denotes spatial second-order cliques (*doubletons* were considered in our experiments) (see Fig. 3), where each clique

corresponds to a pair of neighboring pixels. It is worth mentioning that the spatial energy prior of $\boldsymbol{y_i}$ will be high when its label θ_{y_i} is the same as that of its neighborhood. Similar to (4), in our redefined spatial energy prior, we directly obtain the spatial homogeneity of a determined pixel by considering label continuity between its neighborhood and itself using (7).

Compared with k-means, i.e., hard clustering algorithms, a soft clustering algorithm such as fuzzy *C*-means (FCM) [48] or Gaussian mixing model (GMM) [49] does not assign class labels for points, but defines probabilistic scores per cluster, a.k.a. membership. The closer the data point toward the cluster center, the higher its membership value toward the cluster center. However, many comparative studies and analyses of k-means and soft clustering algorithms, e.g., FCM, for example, [50], [51], show that the soft clustering algorithms offer trivial improvement in experimental performance over k-means while requiring more computational time. In this regard, we give priority to the computational burden; hence, we select k-means for its lower computational cost and guaranteed clustering performance.

It is worth mentioning that we use k-means to initialize class labels for each pixel for spatial energy prior calculation, such that a local area with consistent class labels has high spatial homogeneity, i.e., high spatial energy. Superpixels are local homogeneous areas comprised of a set of spatially correlated and spectrally similar pixels, where pixels originating from the same superpixel are labeled as the same class. The SENMAV algorithm seems to similarly exploit the idea of superpixels, since it uses k-means to preferably capture endmember candidates with high spatial energy. A superpixel algorithm could theoretically provide multiple homogeneous areas in which pixels derived from the same superpixel have high spatial energy as well. However, k-means assigns a unique class label for each pixel, which can characterize local homogeneity between each pixel and its neighborhoods. In this regard, once there exist small targets or anomalous areas, their contributions to the latter tasks will be reduced by considering their inconsistent class label distributions around themselves. Furthermore, such small targets or anomalous areas are problematic for superpixel algorithms, e.g., simple linear iterative clustering [52], to define or characterize, owing to their algorithmic structures. More concretely, such small targets or anomalous areas may be allocated class labels that are the same as the class label of their surroundings within the same superpixel.

B. Maximum Simplex Volume

Based on the pure pixel assumption, the endmembers correspond to the spectral signatures that can define a maximum simplex volume among all the volumes with the vertices specified by other interior pixels. Let $\phi_{\text{spectral}}(\hat{\boldsymbol{y}}_{k_1}, \hat{\boldsymbol{y}}_{k_2}, \ldots, \hat{\boldsymbol{y}}_{k_p})$ be the simplex volume with respect to $\hat{\boldsymbol{y}}_{k_1}, \hat{\boldsymbol{y}}_{k_2}, \ldots, \hat{\boldsymbol{y}}_{k_p}$. Then, the simplex volume can be defined by

$$\phi_{\text{spectral}}\left(\hat{\boldsymbol{y}}_{k_1}, \hat{\boldsymbol{y}}_{k_2}, \ldots, \hat{\boldsymbol{y}}_{k_p}\right) = abs\left(\begin{vmatrix} 1 & 1 & \cdots & 1 \\ \hat{\boldsymbol{y}}_{k_1} & \hat{\boldsymbol{y}}_{k_2} & \cdots & \hat{\boldsymbol{y}}_{k_p} \end{vmatrix}\right) \Big/ (p-1)! \tag{8}$$

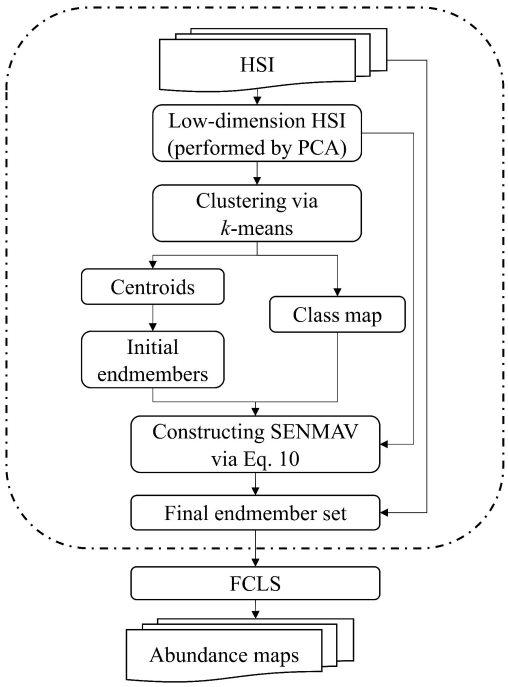

Fig. 4. Diagram of proposed SENMAV algorithm.

where $\hat{\boldsymbol{y}}_{k_1}, \hat{\boldsymbol{y}}_{k_2}, \ldots, \hat{\boldsymbol{y}}_{k_p}$ are pixels selected from $\hat{\mathbf{Y}}$, and $|\cdot|$ denotes the determinant operation. By iteratively searching pixels one-by-one from $\hat{\mathbf{Y}}$ to maximize the simplex volume, we can obtain an increasing simplex volume until it reaches its maximum; the procedure can be formulated as

$$\boldsymbol{V} = \underset{\hat{\boldsymbol{y}}_{k_1}, \hat{\boldsymbol{y}}_{k_2}, \ldots, \hat{\boldsymbol{y}}_{k_p}}{\arg\max}\ \phi_{\text{spectral}}\left(\hat{\boldsymbol{y}}_{k_1}, \hat{\boldsymbol{y}}_{k_2}, \ldots, \hat{\boldsymbol{y}}_{k_p}\right) \tag{9}$$

where $\boldsymbol{V}$ is the maximum simplex volume. A detailed analysis of the maximum simplex volume can be found in Winter [15] and Chang *et al.* [16].

C. SENMAV Framework

The SENMAV algorithm is based on the spatial energy prior and maximum simplex volume. The spatial energy prior is used as a regularization term coupled with the maximum simplex volume model to constrain the selection of the endmembers. The objective function considers (7)–(9), and is given by

$$\boldsymbol{J} = \underset{\hat{\boldsymbol{y}}_{k_1}, \ldots, \hat{\boldsymbol{y}}_{k_i}, \ldots, \hat{\boldsymbol{y}}_{k_p}}{\arg\max} \left\{ \alpha \phi_{\text{spectral}}\left(\hat{\boldsymbol{y}}_{k_1}, \ldots, \hat{\boldsymbol{y}}_{k_i}, \ldots, \hat{\boldsymbol{y}}_{k_p}\right) + \frac{\lambda}{p} \sum_{i=1}^{p} \phi_{\text{spatial}}\left(\hat{\boldsymbol{y}}_{k_i}\right) \right\} \tag{10}$$

where $\alpha = 10^{-\lfloor \log_{10} \boldsymbol{V}_{\lambda=0} \rfloor - 1}$ is a scaling factor that tunes the data scale between $\phi_{\text{spectral}}(\hat{\boldsymbol{y}}_{k_1}, \ldots, \hat{\boldsymbol{y}}_{k_i}, \cdots \hat{\boldsymbol{y}}_{k_p})$ and $\phi_{\text{spatial}}(\hat{\boldsymbol{y}}_{k_i})$. It is an adaptive scaling factor defined by the initial maximum simplex volume $\boldsymbol{V}_{\lambda=0}$ when λ is fixed at 0 (i.e., the spatial energy prior is not taken into account). λ is a spatial regularization factor that weighs the importance of the

Algorithm 1: Pseudocode of the Proposed SENMAV Algorithm.

Input: The hyperspectral data $\mathbf{Y} = [\boldsymbol{y_1}, \boldsymbol{y_2}, \ldots, \boldsymbol{y_n}]_{B\times n}$, the estimated number of endmembers p, the spatial regularization factor λ.
Output: Extracted endmember matrix $\mathbf{M}$

function SENMAV$\mathbf{Y}, p, \lambda$
  $\hat{\mathbf{Y}} \leftarrow PCA(\mathbf{Y}, p-1)$;
  $[\boldsymbol{\theta}, \boldsymbol{\Psi}] \leftarrow kmeans(\hat{\mathbf{Y}}, 2p)$;
  $\boldsymbol{idx} \leftarrow randomperm(2p, p)$;
  $\mathbf{E} \leftarrow \boldsymbol{\Psi}(\boldsymbol{idx}, :)^T$;
  $J_0 \leftarrow \phi_{spectral}(\boldsymbol{E})$;
  for $i = 1 \rightarrow n$ **do**
    for $j = 1 \rightarrow p$ **do**
      $\mathbf{E\_AUX} \leftarrow \mathbf{E}$;
      $\mathbf{E\_AUX}(:, k) \leftarrow \hat{\mathbf{Y}}(:, i)$;
      $\boldsymbol{V}(j) \leftarrow \phi_{spectral}(\mathbf{E\_AUX})$;
    end for
    $[V\_max, idx\_aux] \leftarrow max(\boldsymbol{V})$;
    if $V\_max > J_0$ **then**
      $J_0 \leftarrow V\_max$;
      $\mathbf{E}(:, idx\_aux) \leftarrow \hat{\mathbf{Y}}(:, i)$;
    end if
  end for
  $\alpha \leftarrow 10^{-\lfloor \log_{10} J_0 \rfloor - 1}$;
  $\mathbf{E} \leftarrow \boldsymbol{\Psi}(\boldsymbol{idx}, :)^T$;
  $J_0 \leftarrow \phi_{spectral}(\boldsymbol{E})$;
  for $i = 1 \rightarrow n$ **do**
    for $j = 1 \rightarrow p$ **do**
      $\mathbf{E\_AUX} \leftarrow \mathbf{E}$;
      $\mathbf{E\_AUX}(:, k) \leftarrow \hat{\mathbf{Y}}(:, i)$;
      $\boldsymbol{IDX\_AUX} \leftarrow \boldsymbol{idx}$;
      $\boldsymbol{IDX\_AUX}(j) \leftarrow i$;
  $\boldsymbol{V}(j) \leftarrow \alpha\phi_{spectral}(\mathbf{E\_AUX}) + \frac{\lambda}{p}$ SEP $\boldsymbol{IDX\_AUX}, \boldsymbol{\theta}$;
    end for
    $[V\_max, idx\_aux] \leftarrow max(\boldsymbol{V})$;
    if $V\_max > J_0$ **then**
      $J_0 \leftarrow V\_max$;
      $\mathbf{E}(:, idx\_aux) \leftarrow \hat{\mathbf{Y}}(:, i)$;
      $\boldsymbol{idx}(idx\_aux) \leftarrow i$;
    end if
  end for
  $\mathbf{M} \leftarrow \mathbf{Y}(:, \boldsymbol{idx})$
end function

spatial energy prior. The objective function starts with initial endmembers randomly selected from $\boldsymbol{\Psi}$.

D. SENMAV Description

The endmember extraction mechanism in an HSI is generally seen as searching for the purest pixels, which are based on two important ideas: they are more likely to be found in homogeneous regions; and they reside in the vertices of the data simplex. As seen in Section II, most spectral-based or spatial-spectral-based EEAs depend on one of the abovementioned two ideas.

Algorithm 2: Pseudocode of the Spatial Energy Prior (SEP) Algorithm.

Input: The indices of the endmember candidates: $\boldsymbol{IDX\_AUX}$; initial class map: $\boldsymbol{\theta}$.
Output: the spatial energy prior of the endmember candidates: $\boldsymbol{S}$

function SEP$\boldsymbol{IDX_AUX}, \boldsymbol{\theta}, \mathbf{IDX}$
  $\boldsymbol{S} \leftarrow zeros(length(\boldsymbol{IDX\_AUX}), 1)$;
  for $i = 1 \rightarrow length(\boldsymbol{IDX\_AUX})$ **do**
    $S\_aux \leftarrow 0$;
    $cent \leftarrow \boldsymbol{\theta}(\boldsymbol{IDX\_AUX}(i))$;
    for $j = 1 \rightarrow \kappa$ **do** //κ is a default setting which denotes the number of pixels in the neighborhood system.
      if $cent == \boldsymbol{\theta}(\boldsymbol{IDX\_AUX}(i))_j^{nei}$ **then** // $\boldsymbol{\theta}(\boldsymbol{IDX\_AUX}(i))_j^{nei}$ denotes the classes of neighborhoods related to their central pixel.
        $S\_aux \leftarrow S\_aux + 0$;
      else
        $S\_aux \leftarrow S\_aux + 1$;
      end if
    end for
    $\boldsymbol{S}(i) \leftarrow \exp(-S\_aux)$;
  end for
end function

Therefore, we propose the SENMAV algorithm, which identifies the endmembers by simultaneously considering its spectral features and spatial contextual. The endmembers in our SENMAV framework (10) obtain their spectral information under the data simplex via a maximum simplex volume framework (8) and (9), and the spatial information of the endmembers is acquired by means of the spatial energy prior (7). It is worth mentioning that both terms (i.e., spatial energy prior and maximum simplex volume) have different data scales and make different contributions to select endmembers. For example, the spectral term may reach as low as 10^{-17} (for the *Cuprite* dataset), but the spatial term varies from 0 to 1. Therefore, the scaling factor α and regularization factor λ are invoked to unify the data scales and control the importance of the spatial information.

As Fig. 4 shows, we first reduce the original HSI to a low dimension by the PCA method. Then, we group the dimensionality-reduced HSI into a class map via *k*-means, which captures the spatial energy prior of the endmember candidates, and the initial endmember candidates can be randomly selected from the centroids derived from the clustering stage. Based on the spatial energy prior constrained simplex volume framework, the endmembers can finally be searched until they form maximum objective function values. For the extracted endmembers, fully constrained least squares (FCLS) [19] is utilized to estimate corresponding abundances.

Furthermore, we detail the pseudocode of SENMAV (see Algorithm 1), and the subfunction related to the spatial energy prior is given in Algorithm 2.

E. Computational Complexity Analysis

This section details the computational complexity of SENMAV. First, we capture low-dimension hyperspectral data reduced by the PCA, whose computational complexity is $nB^2/2 + nB(p-1)$. Second, *k*-means yields an initial class map of the dataset, whose computational complexity is reflected by the whole data scale, iteration times, and number of predetermined clusters, and its computational complexity is nlt. The computational complexity of dimension reduction and the *k*-means steps is relatively small and, therefore, is not considered. Third, the maximum simplex volume is needed to specify α. This requires np computations of the determinant of a $p \times p$ matrix, each with complexity $p^{\eta}(2.3 \leq \eta \leq 2.9)$ [53]. Finally, (10) is evaluated to search endmembers, where the determinant and spatial energy prior are executed np times. Each time, the computational complexity of the spatial energy prior of the endmember candidates is sp, where s is the number of pixels in the neighborhood system. Therefore, the approximate computational complexity of SENMAV is $\mathcal{O} = np^{\eta+1} + np(p^{\eta} + sp) = 2np^2(s + p^{\eta-1})$.

F. Endmember Uncertainty Analysis

HU decomposes mixed pixels into a set of endmembers and corresponding proportions, which is an inverse problem, with an infinite number of solutions. However, for most endmember extraction techniques, the endmembers are not blindly separated from mixed pixels via blind source separation methods, but are identified by specifying the vertices or boundary pixels of the data simplex, resulting in negligible endmember uncertainty. It is worth mentioning that such light endmember uncertainty does not maintain the accuracy propagation of abundance estimation performance, owing to several factors. The first factor lies in the algorithmic structural defects. For instance, maximal volume-based algorithms (e.g., N-FINDR, SGA, AVMAX, and SENMAV) maximize a determinant for endmember extraction purposes, yet the calculation of the determinant is normally nonconvex, leading to an inconsistent solution. In addition, simplex projection-based algorithms (e.g., VCA) demand substantial random vectors to capture the extreme projections of hyperspectral data; hence, the extracted endmembers are not stable. The second factor may owe to spectral variability because the spectral signatures of observed land cover are inconsistent due to illumination and atmospheric conditions. In this case, the endmember uncertainty will increase. For SENMAV and other maximal volume and extreme projection-based EEAs, although the light endmember uncertainty may lead to potential error propagation, they still could be used for their clear conceptual meaning, acceptable endmember accuracy, and light computational burden. A detailed analysis of the endmember uncertainty can be found in Zhou *et al.* [54] and Ozkan and Akar [55].

IV. Results

Several experiments were conducted on synthetic and real hyperspectral datasets. Five state-of-the-art EEAs were used to evaluate the performance of the proposed algorithm. VCA [14], AVMAX [17], and MVSA [23] are spectral based, and AMEE [29] and SSEBE [27] are spatial-spectral based. All the algorithms ran on a PC with an Intel core i7-2600 K (at 3.40 GHz) and 8GB RAM.

A. Evaluation Metrics

Two well-known benchmark metrics, spectral angle distance (SAD) and root-mean-square error (RMSE), were adopted to assess the performance of all considered EEAs. SAD was used to evaluate the spectral similarity between observed spectra and the spectra library, and is given by

$$\text{SAD}\left(\boldsymbol{y_i}, \boldsymbol{y_j}\right) = \arccos\left(\frac{\boldsymbol{y_i}^T \boldsymbol{y_j}}{\|\boldsymbol{y_i}\| \, \|\boldsymbol{y_j}\|}\right). \tag{11}$$

The higher the spectral similarity between two spectra, the smaller the SAD. The RMSE is used to evaluate the image reconstruction error between the original and reconstructed HSI determined by the extracted endmembers and the corresponding estimated abundancies, and it is defined as

$$\text{RMSE}\left(\mathbf{Y}, \tilde{\mathbf{Y}}\right) = \sqrt{\frac{1}{B \times n} \sum_{i=1}^{n} \left(\boldsymbol{y_i} - \tilde{\boldsymbol{y}}_{\boldsymbol{i}}\right)^2} \tag{12}$$

where $\boldsymbol{y_i}$ and $\tilde{\boldsymbol{y}}_{\boldsymbol{i}}$ are derived from the original HSI and the reconstructed HSI, respectively. The lower the RMSE, the better the reconstruction performance.

Additionally, the Davies–Bouldin index (DBI) [56] is used to evaluate the clustering performance of *k*-means on the initial class map generation process. The DBI calculates the maximum index according to the sum of the average intradistance of any two categories divided by the distance between two clustering centers. The greater the index, the better the clustering result. It is given as

$$\text{DBI} = \frac{1}{N} \sum_{i} \max_{j, j \neq i} \left\{ \left[\frac{1}{n_i} \sum_{x \in C_i} d\left(x, c_i\right) + \frac{1}{n_j} \sum_{x \in C_j} d\left(x, c_j\right) \right] \Big/ d\left(c_i, c_j\right) \right\} \tag{13}$$

where x, N, C_i, n_i, c_i, and $d(c_i, c_j)$ are, respectively, the data point, number of clusters, *i*th cluster, number of objects in C_i, center of C_i, and distance between c_i and c_j.

B. Experimental Dataset Descriptions

1) Synthetic Dataset Without Outliers (DS1): For the synthetic dataset, five endmembers were randomly selected from the United States Geological Survey (USGS) spectral library[1] with 224 bands. These are *Alunite*, *Dumortierite*, *Nontronite*, *Sphene*, and *Kaolinite*. A well-known HSI generation toolbox[2] was used to generate a 100 × 100 pixel synthetic image based

[1] http://speclab.cr.usgs.gov/spectral.lib06

[2] http://www.ehu.es/ccwintco/index.php/Hyperspectral_Imagery_Synthesis_tools_for_MATLAB

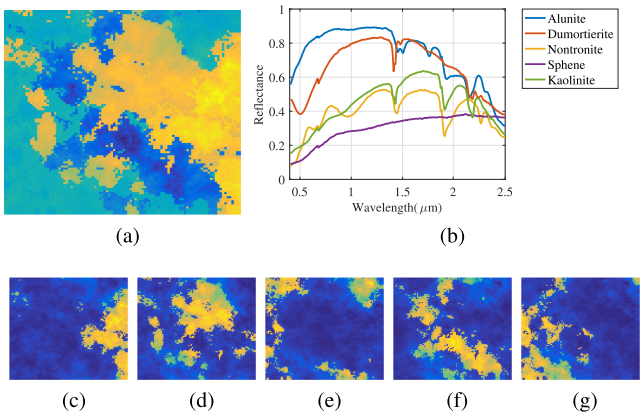

Fig. 5. (a) Hyperspectral synthetic image (100th bands) without outlier. (b) Five spectral signatures. (c)–(g) Abundance maps related to each spectral signature.

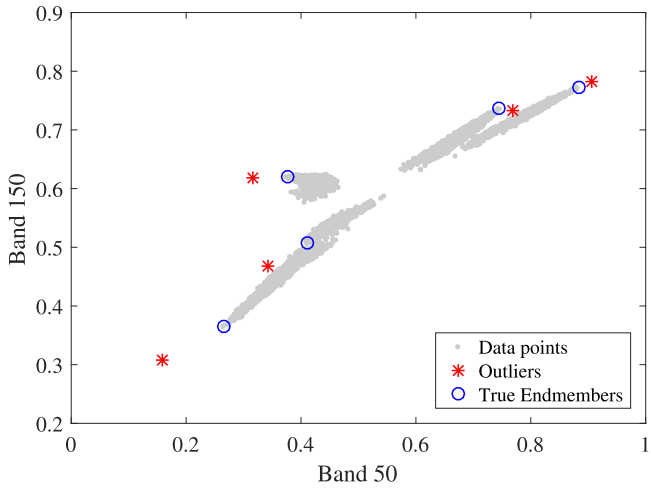

Fig. 6. Scatter plot of *DS2*. Gray points, blue circles, and red stars denote normal data points, endmembers, and outliers, respectively.

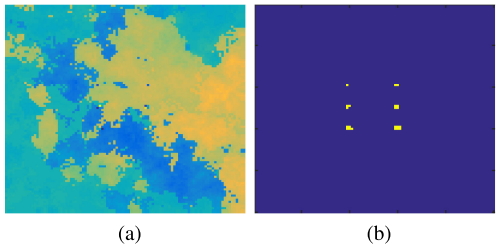

Fig. 7. (a) Hyperspectral synthetic dataset (100th bands) with different spatial structure of outliers. (b) Positions of outliers.

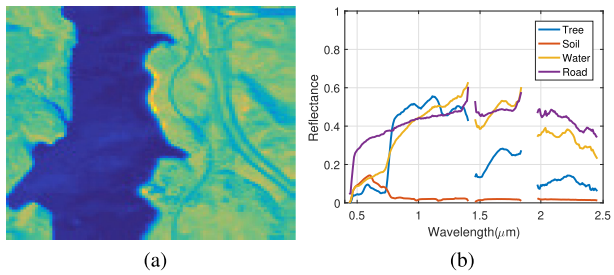

Fig. 8. (a) Japser Ridege dataset (100th band). (b) Four endmembers.

on LMM, ANC, ASC, and pure pixel assumptions, and the selected endmembers. Fig. 5 displays the synthetic dataset (100th band) with its corresponding five endmember signatures and abundance maps. Zero-mean white Gaussian noise was added to the synthetic images with signal-to-noise ratios (SNRs) varying from 20 to 40 dB, with stepwise increases of 5.

2) Synthetic Dataset With Single Outlier per Area (DS2): To test the algorithms on a more realistic case, five outliers with different mixing levels were randomly added to *DS1*. In [57], the outliers are considered to be the pixels that appear to deviate markedly from the rest of the data, where the spectral reflectance of several consecutive bands is significantly higher than that of other bands. In [58] and [33], the outliers are regarded as the pixels far from the data simplex. Based on LMM (1), we accepted the latter idea and formulated an outlier spectrum $\boldsymbol{a}$, as follows:

$$\boldsymbol{a} = \boldsymbol{m_p}\gamma + \mathbf{U_{p-1}}\boldsymbol{\zeta_{p-1}} + \boldsymbol{\omega} \tag{14}$$

where $\gamma \in [1, 1.2]$ denotes the abundance fraction of a desired target spectrum $\boldsymbol{m_p}$, and $\gamma + \mathbf{1}^{\boldsymbol{T}}\boldsymbol{\zeta_{p-1}} = 1$, where $\mathbf{1}$ is a $p \times 1$ vector of ones. Fig. 6 presents the positions of the data points along with the endmembers and outliers. For each area covered by a specified endmember, there exists a corresponding outlier to simulate the real situation.

3) Synthetic Dataset With Multiple Outliers per Area (DS3): Unlike $DS2$, the outliers were fixed with different spatial structures in $DS3$. Six panels of different spatial structures randomly filled with outliers were added to the image (see Fig. 7).

4) Japser Ridge Hyperspectral Dataset: Japser Ridge [59] is a popular real hyperspectral dataset used in the unmixing field (see Fig. 8). The original *Japser Ridge* image contains 512×614 pixels with 224 spectral bands. In this article, a subimage of 100×100 pixels with 198 bands is considered (owing to dense water vapor and atmospheric effects, bands 1–3, 108–112, 154–166, and 220–221 are removed). Four endmembers, i.e., *Road*, *Soil*, *Water*, and *Tree*, are observed from this dataset.

5) Cuprite Hyperspectral Dataset: Cuprite is a well-known benchmark hyperspectral dataset for HU (see Fig. 9), with data captured by the Airborne Visible Infrared Imaging Spectrometer (AVIRIS) in Las Vegas, NV, USA. A 250×190 pixel subset with 182 bands was used in this experiment[3] (the noise and water absorption bands were removed from 224 bands, and the excluded bands were 1–6, 105–115, 150–170, and 221–224), where there were 14 types of minerals estimated by the hyperspectral signal identification by minimum error (Hysime) [60]. Based on the analysis in the literature [61], there are minor differences between variants of similar minerals; hence, 12 minerals were considered in the experiment: *Alunite*, *Andradite*, *Buddingtonite*, *Dumortierite*, *Kaolinite#1*, *Kaolinite#2*, *Muscovite*, *Montmorillonite*, *Nontronite*, *Pyrope*, *Sphene*, and *Chalcedony*.

[3]http://aviris.jpl.nasa.gov/html/aviris.freedata.html

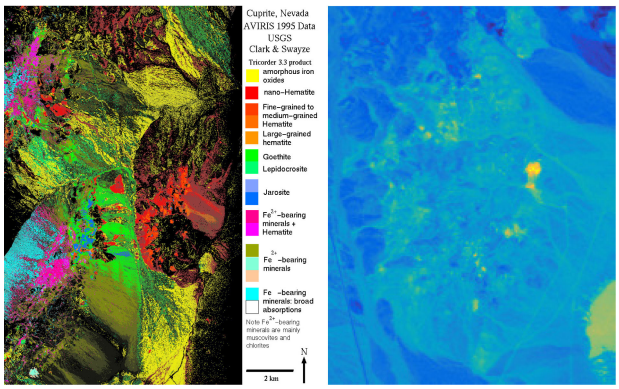

Fig. 9. (a) USGS map with different minerals in a cuprite mining district in Las Vegas, NV, USA. (b) *Cuprite* dataset (100th band) sized 250 × 190 pixels, which is a subset of the USGS map.

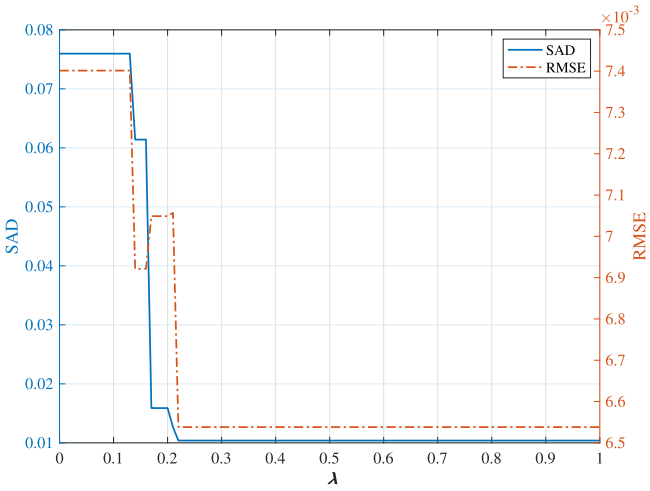

Fig. 10. Impact of λ on SAD and RMSE.

C. Experimental Performance

1) Experiment 1 (Parameter Tuning): In this article, the proposed SENMAV algorithm involves only one parameter, the spatial regularization factor λ. Therefore, the aim of this experiment was to verify the impact of λ on the performance. *DS*2 was used to perform the experiment (with SNR fixed at 40 dB) since it contains several outliers. As we can see from Fig. 10, when λ varies from 0 to 1, the SAD and RMSE results change significantly, indicating that λ plays an important role in avoiding outliers for SENMAV. According to Fig. 10, we fixed λ at 0.4 for the experiments. Based on the fixed λ, Fig. 11 plots the data points, outliers, true endmembers, and extracted endmembers, and shows that SENMAV precisely searches the positions of the endmembers under the interference of outliers.

2) Experiment 2 (Evaluation of k-Means on Initial Class Map Generation Process): To validate the effect of the number of clusters l on the performance, this experiment was conducted on the *Cuprite* dataset. Fig. 12 plots the DBI on different numbers of clusters varying from 1 to 30. A high DBI means good clustering

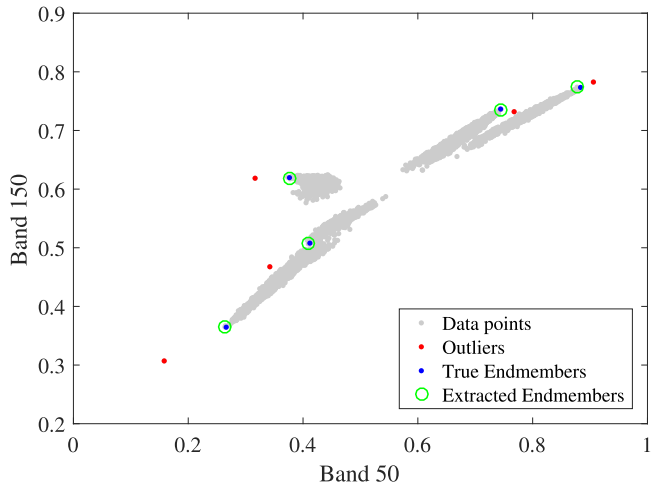

Fig. 11. Scatter plot of data points (gray points), outliers (red points), true endmembers (blue points), and extracted endmembers (green circles).

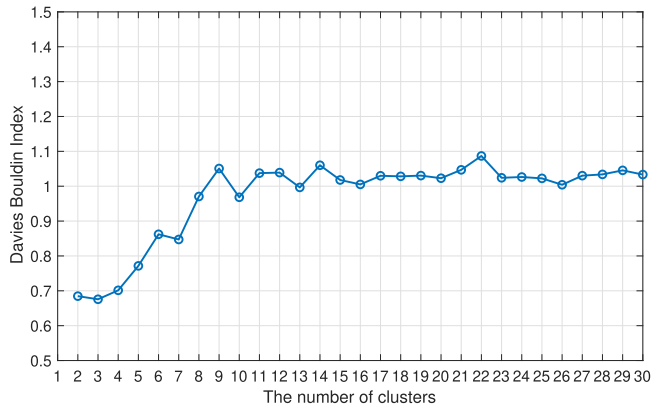

Fig. 12. DBI on different numbers of clusters.

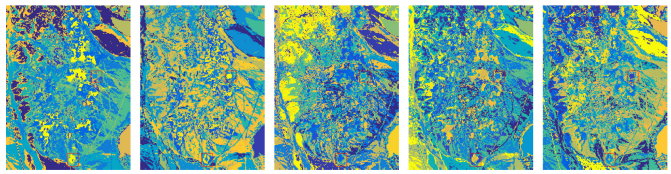

Fig. 13. Clustering maps. (a) 14 clusters. (b) 18 clusters. (c) 22 clusters. (d) 26 clusters. (e) 30 clusters.

performance. As Fig. 12 shows, the number of clusters in the interval [14, 28] (14 is regarded as the number of estimated endmembers) displays relatively stable Davies– Bouldin results, where 22 clusters can yield the best clustering performance. Fig. 13(a), (b), (c), (d), and (e) show clustering maps related to 14, 18, 22, 26, and 30 clusters, respectively. Two red rectangles in each figure indicate the range of two representative minerals, *muscovite* and *dumortierite*. As can be seen from Fig. 13(a) and (b), when the number of clusters is large, the spatial homogeneity may be reduced due to inconsistent class labels.

TABLE I
SAD RESULTS BETWEEN EXTRACTED ENDMEMBERS AND CORRESPONDING USGS LIBRARY ON *DS1*

Algorithms	VCA	AVMAX	MVSA	AMEE	SSEBE	SENMAV
Alunite	0.0013	0.0072	0.0029	0.0455	0.0179	0.0072
Dumortierite	0.0009	0.0084	0.0031	0.2332	0.0078	0.0084
Nontronite	0.0010	0.0127	0.0030	0.1691	0.0222	0.0127
Sphene	0.0020	0.0166	0.0186	0.0507	0.2002	0.0166
Kaolinite	0.0015	0.0125	0.0058	0.1527	0.0150	0.0107
Mean	0.0013	0.0115	0.0067	0.1302	0.0526	0.0111

TABLE II
SAD RESULTS BETWEEN EXTRACTED ENDMEMBERS AND CORRESPONDING USGS LIBRARY ON *DS2*

Algorithms	VCA	AVMAX	MVSA	AMEE	SSEBE	SENMAV
Alunite	0.0226	0.0236	0.0230	0.0463	0.0159	0.0074
Dumortierite	0.0171	0.0188	0.0319	0.4708	0.0074	0.0074
Nontronite	0.0668	0.0681	0.0632	0.1680	0.0206	0.0117
Sphene	0.1855	0.1865	0.2332	0.0512	0.0525	0.0154
Kaolinite	0.0819	0.0828	0.1014	0.1516	0.0217	0.0100
Mean	0.0748	0.0760	0.0906	0.1776	0.0236	0.0104

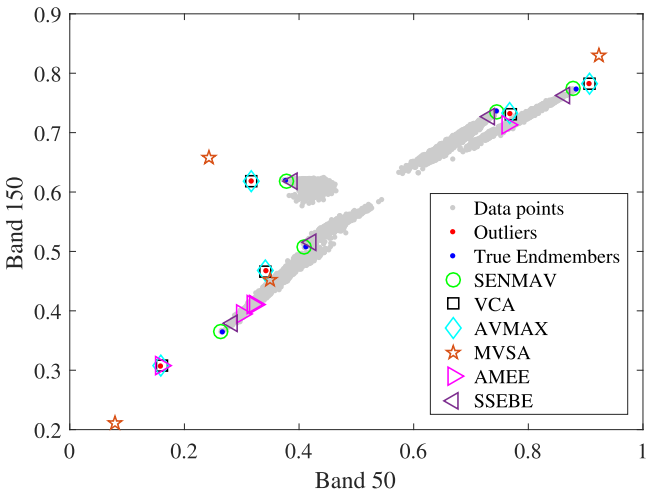

Fig. 14. Scatter plot of endmembers extracted by all EEAs.

TABLE III
TIME CONSUMPTION (IN *SECONDS*) ON *DS1*, *DS2*, AND *DS3* WITH SNR FIXED AT 40 DB

Algorithm	VCA	AVMAX	MVSA	AMEE	SSEBE	SENMAV
DS1	0.09	0.04	1.13	91.13	2.67	3.30
DS2	0.16	0.04	3.41	90.70	2.53	3.31
DS3	0.09	0.04	2.00	90.52	2.16	3.32

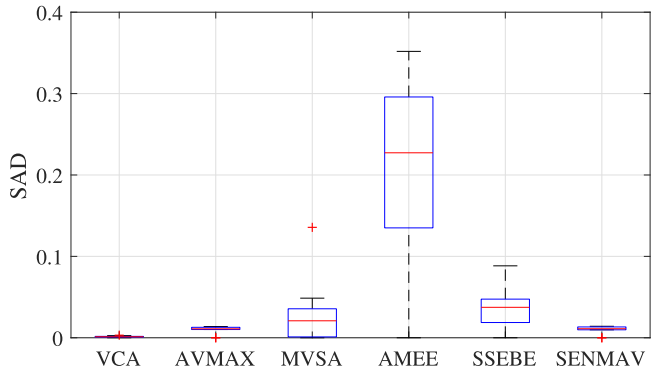

Fig. 15. Box plot of SAD results of all EEAs on synthetic datasets with number of endmembers varying from 3 to 10.

3) Experiment 3 (Endmember Extraction Performance of EEAs): This experiment evaluated the endmember extraction performance associated with five endmembers on $DS1$, while containing the same noise (fixed at 40 dB). Table I lists the data on the SAD results between the extracted endmembers and the corresponding USGS library. From the table, we can see that SENMAV can provide almost the same extraction performance as AVMAX, and better than AMEE and SSEBE, on five endmembers. This indicates that SENMAV well captures the superiority of the simplex at identifying endmembers. It should be noted that VCA offers mostly low SAD values on all the endmembers, mainly due to its specific endmember extraction mechanism on noisy data.

4) Experiment 4 (Impact of Outliers on EEAs): To validate the impact of outliers on all the EEAs, this experiment was performed based on *DS2*, with SNR fixed at 40 dB. As shown in Fig. 14, the endmembers extracted by SENMAV (green circle) were located at the position of true endmembers (blue points). However, most of the comparison EEAs, e.g., VCA (black rectangular) and AVMAX (cyan diamond), regard outliers (red points) as endmembers. For the MVSA algorithm (orange five-pointed star), the simplex structure is obstructed by the outliers, with the result that the generated endmembers deviate from true endmembers. The spatial-spectral-based algorithms AMEE (pink right-triangle) and SSEBE (brown left-triangle) could somewhat avoid interference of outliers because they exploit the spatial correlations between pixels. Table II lists corresponding numerical results, which demonstrate that SENMAV still provided accurate endmember identification results while comparison algorithms mistakenly extracted the endmembers. To analyze the time consumption of the EEAs on the synthetic datasets, we recorded the execution time (in *seconds*) of the EEAs on *DS1*, *DS2*, and *DS3*, with the SNR fixed at 40 dB (see Table III). We observe from Table III that most EEAs took less time than AMEE, which requires a dynamically spatial sliding kernel window with many dot products to identify the purest pixels.

5) Experiment 5 (Evaluation of Different Numbers of Endmembers): To test the robustness of the EEAs on different numbers of endmembers, this experiment varied the number of endmembers from 3 to 10, with HSI sized 100×100 and noise fixed at 40 dB. Based on the SAD results obtained from the EEAs on these synthetic images (each image contains different endmembers), Fig. 15 shows a box plot of the SAD results. Compared with AMEE and SSEBE, SENMAV maintained small SAD variability on all the synthetic images with different endmember number scenarios, as did VCA and AVMAX, which implies that SENMAV was robust to the endmember number.

6) Experiment 6 (Comparison Between SENMAV and Other Algorithms Under Different Noise and Dataset Scenarios): To assess the impact of different noise and dataset scenarios, experiment 5 was executed by all the algorithms, and the results were averaged on ten independent experiments. It can be seen from

TABLE IV
SAD RESULTS OBTAINED BY ALL COMPARISON ALGORITHMS UNDER DIFFERENT NOISE AND DATASET SCENARIOS

Algorithms		VCA	AVMAX	MVSA	AMEE	SSEBE	SENMAV
DS1	**20 dB**	0.0178	0.1166	0.1885	0.1872	0.1475	0.1110
	25 dB	0.0100	0.0629	0.1419	0.2117	0.1439	0.0628
	30 dB	0.0045	0.0354	0.0454	0.1918	0.1130	0.0355
	35 dB	0.0022	0.0202	0.0197	0.1356	0.0654	0.0198
	40 dB	0.0013	0.0122	0.0067	0.1302	0.0258	0.0111
	Mean	0.0071	0.0495	0.0804	0.1713	0.0991	0.0480
DS2	**20 dB**	0.0728	0.1382	0.2777	0.2925	0.1394	0.1123
	25 dB	0.0720	0.1023	0.1164	0.2529	0.1446	0.0656
	30 dB	0.0725	0.0837	0.1130	0.2391	0.0922	0.0362
	35 dB	0.0738	0.0749	0.0951	0.2375	0.0430	0.0193
	40 dB	0.0745	0.0748	0.0906	0.1776	0.0242	0.0104
	Mean	0.0731	0.0948	0.1385	0.2399	0.0887	0.0488
DS3	**20 dB**	0.0675	0.1299	0.3420	0.3242	0.1394	0.1108
	25 dB	0.0701	0.0827	0.2219	0.2434	0.1489	0.0649
	30 dB	0.0715	0.0648	0.2062	0.2237	0.0931	0.0358
	35 dB	0.0797	0.0628	0.2446	0.2202	0.0294	0.0198
	40 dB	0.0899	0.0541	0.2295	0.2175	0.0242	0.0113
	Mean	0.0757	0.0789	0.2489	0.2458	0.0870	0.0485

TABLE V
OVERALL EXPERIMENTAL RESULTS (SAD, AVERAGE SAD, RMSE, AND EXECUTION TIME) OBTAINED BY ALL COMPARISON ALGORITHMS ON JAPSER RIDGE DATASET

Algorithms	VCA	AVMAX	MVSA	AMEE	SSEBE	SENMAV
Tree	0.1481	0.1559	0.1793	†	**0.0253**	0.1724
Water	0.2582	0.2453	†	**0.0902**	†	0.2453
Dirt	0.1289	0.1336	0.2122	†	0.1265	**0.1233**
Road	0.0901	0.1069	0.0663	†	0.0531	**0.0443**
Mean	0.1563	0.1604	0.1526	0.0902	0.0683	0.1463
RMSE	0.0079	0.0110	**0.0065**	0.1495	0.0983	0.0124
Execution time (s)	0.0847	0.0372	13.2610	36.5752	2.0788	2.3177

† denotes that the mineral is not extracted.

the data in Table IV that SENMAV well maintained endmember extraction accuracy under different noise and dataset scenarios. Most comparison algorithms were only good at specifying endmembers under no outlier assumptions in *DS1*, but in *DS2* and *DS3*, which contain outliers with different scenarios, they had high SAD results, implying that the outliers were extracted. It is noteworthy that SSEBE provides better results than other comparison algorithms on *DS2* and *DS3*, perhaps because SSEBE involves a clustering step, which can alleviate noise or outlier interference.

7) Experiment 7 (Comparison Between SENMAV and Other EEAs on Japser Ridge Dataset): This experiment was conducted on the *Japser Ridge* dataset, and was used to assess the endmember extraction performance of different EEAs on a real dataset scenario the best results are bolded and the suboptimal results are underlined. Table V tabulates overall results including SAD, average SAD, RMSE, and execution time obtained from all EEAs. It can be seen from this table that SENMAV provided relatively better endmember extraction accuracy on both *Dirt* and *Road* ground objects compared to spectral-based EEAs. Also, compared to the spatial-spectral-based EEAs, SENMAV identified four desired endmembers, while both AMEE and SSEBE missed several endmembers. RMSE results in this table show that SENMAV and the other spectral-based algorithms could yield lower reconstruction error than the AMEE and

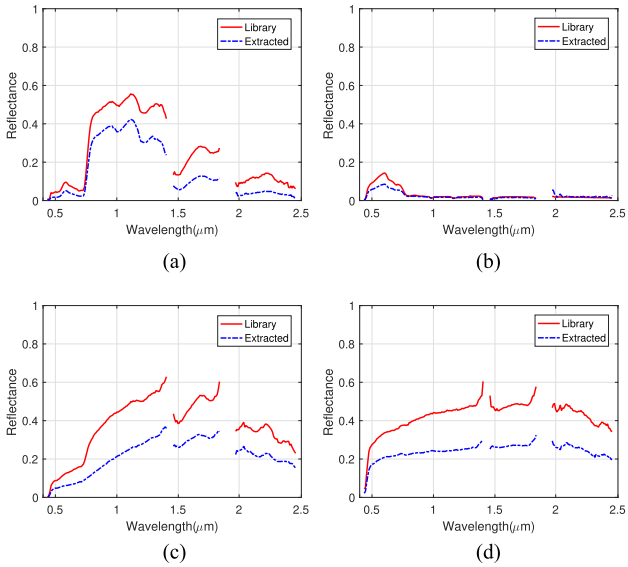

Fig. 16. Visual comparison between extracted endmembers (blue dashed curve) and library spectra (red solid curve). (a) *Tree*. (b) *Water*. (c) *Dirt*. (d) *Road*.

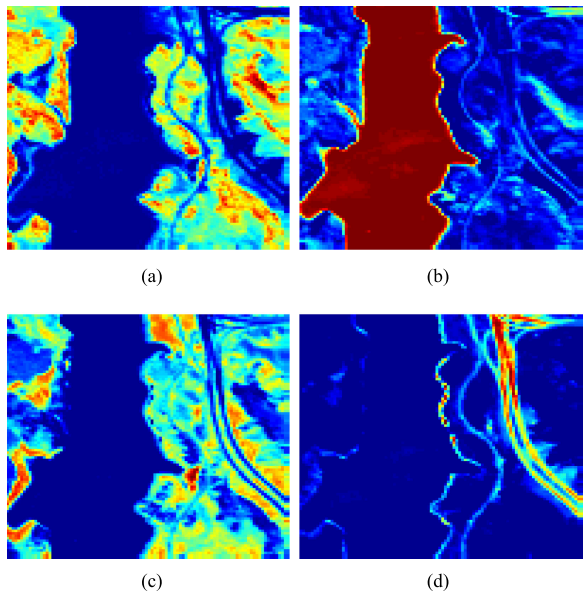

Fig. 17. Estimated abundance maps on *Japser Ridge*. (a) *Tree*. (b) *Water*. (c) *Dirt*. (d) *Road*.

SSEBE algorithms. Execution time from SENMAV was higher than from VCA and AVMAX, yet the computational cost was acceptable compared to MVSA and SSEBE. The identified endmembers were visually compared to the spectral library, which can be found in Fig. 16. The abundances of the identified endmembers are displayed in Fig. 17, as estimated by the FCLS algorithm [19].

8) Experiment 8 (Comparison Between SENMAV and Other EEAs on Cuprite *Dataset):* In this experiment, each algorithm was performed ten times. Based on the RMSE evaluation metric, Fig. 18(a) shows the box plot of the entire RMSE results obtained from the six algorithms on the *Cuprite* dataset with ten independent runs. From this figure, we can see that SENMAV resulted in

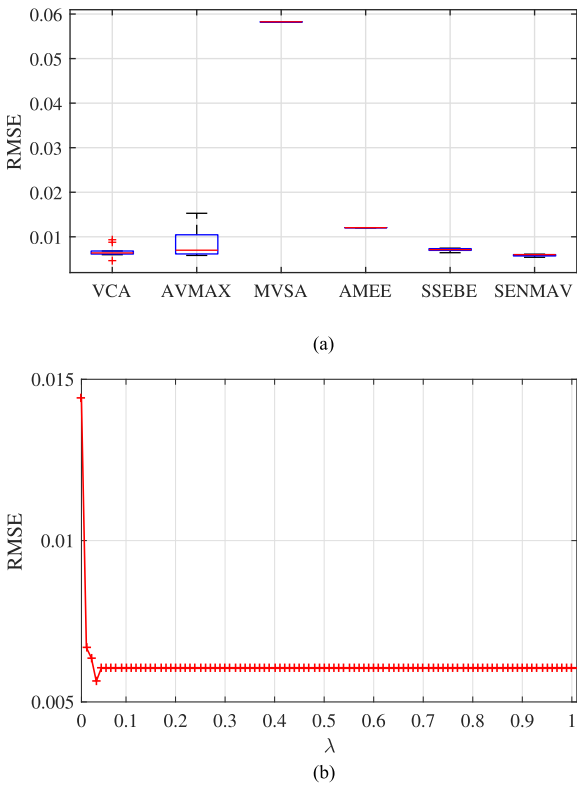

Fig. 18. (a) Box plot of RMSE results obtained from six algorithms with ten independent runs on the *Cuprite* dataset. (b) RMSE result trend with λ varying from 0 to 1.

the lowest and most stable RMSE values on ten runs, indicating that SENMAV could yield relatively consistent experimental results on multiple runs. Furthermore, Fig. 18(b) provides a trend of RMSE results when varying λ. What stands out in this figure is the rapid decrease and then stabilization in RMSE results. It is worth mentioning that the *Cuprite* dataset contains complex topographic features and highly mixed spectral signatures, with the result that the SAD and RMSE results obtained by many EEAs were inconsistent on multiple runs. As we can see from Fig. 18(a), under ten independent runs, the RMSE results obtained from AVMAX displayed great variability. Therefore, for the proposed SENMAV algorithm, when λ is relatively small, the spatial energy prior term will contribute weak constraints to simplex volume, which indicates that the RMSE results may be uncorrelated compared with the RMSE results when λ is larger than 0.1. Similarly, Fig. 10 shows that when λ was smaller than 0.3, the SAD results were high, indicating that the outliers hampered the endmember search process. Additionally, both Figs. 15 and 18(a) use the box plot method to display the distribution features of the experimental results. The first figure shows the SAD results of the EEAs on eight synthetic images (each image has a different endmember number), and the second shows the RMSE results of the EEAs with ten runs on the *Cuprite* dataset.

The overall experimental results, such as SAD, average SAD, RMSE, and execution time (in *seconds*), of all the algorithms performed on the *Cuprite* dataset are set out in Table VI. This table is quite revealing in several ways. First, SENMAV has

TABLE VI
OVERALL EXPERIMENTAL RESULTS (SAD, AVERAGE SAD, RMSE, AND EXECUTION TIME) OBTAINED BY ALL COMPARISON ALGORITHMS ON CUPRITE DATASET

Algorithms	VCA	AVMAX	MVSA	AMEE	SSEBE	SENMAV
Alunite	**0.0783**	0.0898	0.0816	†	0.1058	0.0794
Andradite	0.1638	0.1643	0.0986	0.1248	0.0760	**0.0668**
Buddingtonite	0.0751	**0.0750**	0.1149	0.1337	0.1414	0.1335
Dumortierite	**0.0611**	0.0685	0.0666	0.0647	0.0682	0.0651
Kaolinite#1	0.1196	0.0804	0.0978	0.1035	0.1481	**0.0746**
Kaolinite#2	0.0705	0.0707	**0.0669**	0.0789	0.0788	0.0940
Muscovite	0.0880	0.0863	†	0.1585	0.0752	**0.0750**
Montmorillonite	0.0623	0.0586	†	0.0877	**0.0576**	0.0586
Nontronite	0.0737	**0.0652**	0.0715	†	†	0.0937
Pyrope	0.0576	0.0582	0.1998	0.0876	**0.0501**	0.0582
Sphene	0.0917	0.0915	0.0929	0.0656	**0.0545**	0.0774
Chalcedony	0.1352	0.1004	0.1596	†	0.1223	**0.0880**
Mean	0.0898	0.0841	0.1050	0.1006	0.0889	**0.0804**
RMSE	0.0068	0.0074	0.0583	0.0120	0.0072	**0.0060**
Execution time (s)	0.60	1.62	138.87	159.78	67.54	88.32

an advantage over the other spatial-spectral-based algorithms, AMEE and SSEBE, in specifying several minerals, e.g., *Andradite*, *Kaolinite#1*, *Muscovite*, and *Chalcedony*, without missing any minerals. These results offer compelling evidence that SENMAV may have better endmember extraction performance than the spatial-spectral-based algorithms. Second, compared to the spectral-based EEAs, VCA, AVMAX, and MVSA, SENMAV may require more computational time, but it still provided competitive experimental results such as average SAD or RMSE. Moreover, the extracted endmember signatures are compared to the library spectra in Fig. 19. For most extracted endmembers, they are closely matched to corresponding library spectra. Especially for *Pyrope*, the extracted endmember signatures have low correlations with the library spectra, perhaps owing to the high spectral mixing level. The corresponding abundance maps are summarized in Fig. 20.

V. DISCUSSION

As stated in the introduction, our main aim is to propose a SENMAV algorithm for spatial-spectral hyperspectral endmember extraction. The single most marked observation to emerge from the data comparison is that SENMAV can greatly improve the efficiency and accuracy of endmember extraction for spatial-spectral-based EEAs.

Generally, the spectral-based EEAs, whether simplex projection-based, maximum simplex volume-based, or minimum simplex volume-based, exploit the spectral attributes of the endmembers when discarding their spatial correlations. Therefore, they are sensitive to outliers, which could force a vertex of the simplex to reside at a point beyond the nominal position of the endmember in order to enclose all data points. On the other side, the spatial-spectral-based EEAs heavily resort to a determined combination of spatial and spectral information between pixels to specify endmembers without considering the convexity of the data structure, thus, involving many important parameters to optimize endmember extraction performance. Unfortunately, those parameters demand tuning according to different qualities of dataset scenarios or algorithmic requirements for designation at the price of computation. However, SENMAV

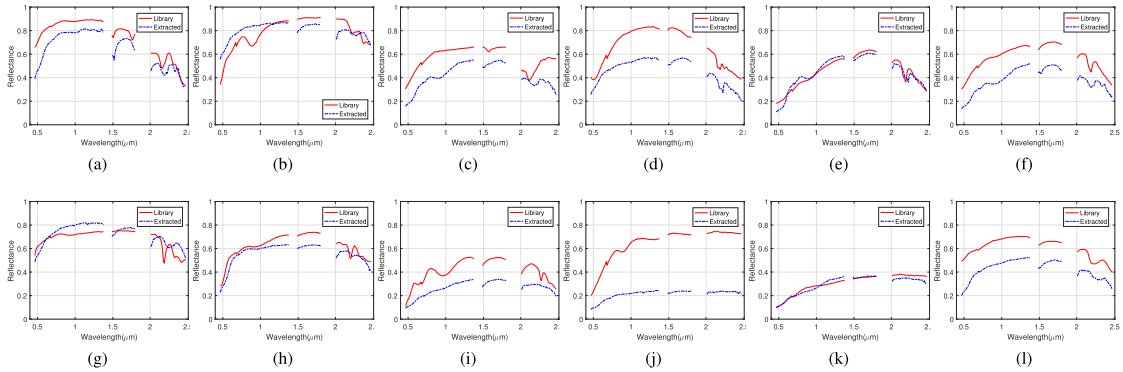

Fig. 19. Visual comparison between extracted endmember and library spectra. (a) *Alunite*. (b) *Andradite*. (c) *Buddingtonite*. (d) *Dumortierite*. (e) *Kaolinite#1*. (f) *Kaolinite#2*. (g) *Muscovite*. (h) *Montmorillonite*. (i) *Nontronite*. (j) *Pyrope*. (k) *Sphene*. (l) *Chalcedony*.

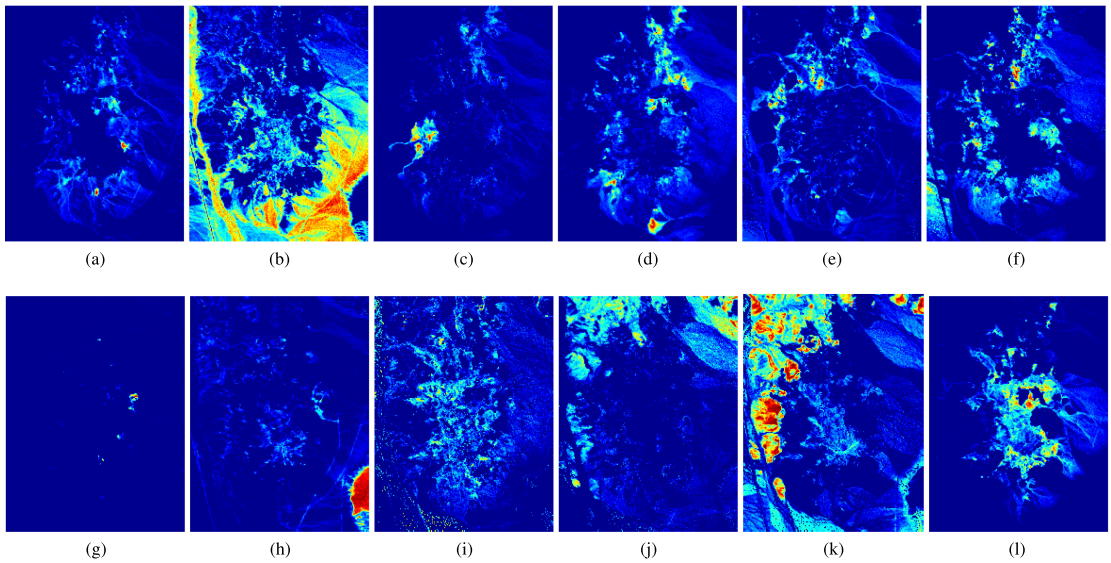

Fig. 20. Abundance maps related to each extracted mineral. (a) *Alunite*. (b) *Andradite*. (c) *Buddingtonite*. (d) *Dumortierite*. (e) *Kaolinite#1*. (f) *Kaolinite#2*. (g) *Muscovite*. (h) *Montmorillonite*. (i) *Nontronite*. (j) *Pyrope*. (k) *Sphene*. (l) *Chalcedony*.

integrates the spatial energy prior and well-known maximum simplex volume framework, which simultaneously obtains the preferable endmember extraction performance of the maximum simplex volume framework and the spatial energy prior to the endmembers to pinpoint the final endmembers. As expected, our experiments demonstrate that SENMAV well controls the tradeoff between endmember extraction efficiency and spatial attributes of endmembers.

We are aware that the computational cost of SENMAV may be on the high side since two important aspects, i.e., maximum simplex framework and spatial energy prior, are governed to jointly exploit the spatial and spectral information of the endmembers. Most importantly, it is costly to determine the adaptive threshold α, which demands a full and independent maximum simplex volume computational task. Moreover, the spatial regularization factor may slightly influence experimental performance according to different HSI scenarios, and this factor is normally tuned in the interval [0, 1].

As mentioned in the introduction, no one appears to have applied current knowledge of the combination of the spatial energy prior and maximum simplex volume framework to the field of spatial-spectral endmember extraction. Therefore, the importance of our experimental results using SENMAV lies both in its efficiency and accuracy in determining the endmembers to the spatial-spectral endmember extraction area.

VI. Conclusion

In this article, we proposed a spatial energy constrained maximum simplex volume approach, SENMAV, for spatial-spectral endmember extraction. SENMAV is a new model in which the transitional maximum simplex volume is regularized by the spatial energy prior, resulting in the identified endmembers capturing the convexity and spatial energy within the data structure and HSI, respectively. Results from experiments comparing SENMAV to other spectral-based and spatial-spectral-based algorithms on synthetic and real hyperspectral datasets point toward the idea that SENMAV has clearly improved endmember extraction performance. These findings add to a growing body of literature on our understanding of spatial-spectral-based endmember extraction. The most important limitation of SENMAV may be its high computational cost, since the maximum simplex

framework and spatial energy prior are governed to jointly exploit the spatial and spectral information of the endmembers. Therefore, investigation is needed to decrease the computational complexity without sacrificing high endmember extraction performance in the field of spatial-spectral hyperspectral endmember extraction.

ACKNOWLEDGMENT

The authors would like to thank the Image and Intelligence Information Processing Innovation Team of the National Ethnic Affairs Commission of China for their support. They would also like to thank the Associate Editor and the three anonymous reviewers for their outstanding comments and suggestions, which greatly improved the technical quality and presentation of this manuscript.

REFERENCES

[1] C. Shi and L. Wang, "Incorporating spatial information in spectral unmixing: A review," *Remote Sens. Environ.*, vol. 149, pp. 70–87, 2014.

[2] J. M. Bioucas-Dias *et al.*, "Hyperspectral unmixing overview: Geometrical, statistical, and sparse regression-based approaches," *IEEE J. Sel. Topics Appl. Earth Observ. Remote Sens.*, vol. 5, no. 2, pp. 354–379, Apr. 2012.

[3] J. M. Bioucas-Dias, A. Plaza, G. Camps-Valls, P. Scheunders, N. Nasrabadi, and J. Chanussot, "Hyperspectral remote sensing data analysis and future challenges," *IEEE Geosci. Remote Sens. Mag.*, vol. 1, no. 2, pp. 6–36, Jun. 2013.

[4] N. Keshava and J. F. Mustard, "Spectral unmixing," *IEEE Signal Process. Mag.*, vol. 19, no. 1, pp. 44–57, Jan. 2002.

[5] S. Ozkan, B. Kaya, and G. B. Akar, "EndNet: Sparse autoencoder network for endmember extraction and hyperspectral unmixing," *IEEE Trans. Geosci. Remote Sens.*, vol. 57, no. 1, pp. 482–496, Jan. 2019.

[6] X. Zhang, Y. Sun, J. Zhang, P. Wu, and L. Jiao, "Hyperspectral unmixing via deep convolutional neural networks," *IEEE Geosci. Remote Sens. Lett.*, vol. 15, no. 11, pp. 1755–1759, Nov. 2018.

[7] M.-D. Iordache, J. M. Bioucas-Dias, and A. Plaza, "Sparse unmixing of hyperspectral data," *IEEE Trans. Geosci. Remote Sens.*, vol. 49, no. 6, pp. 2014–2039, Jun. 2011.

[8] M.-D. Iordache, J. M. Bioucas-Dias, and A. Plaza, "Total variation spatial regularization for sparse hyperspectral unmixing," *IEEE Trans. Geosci. Remote Sens.*, vol. 50, no. 11, pp. 4484–4502, Nov. 2012.

[9] J. Huang, T.-Z. Huang, L.-J. Deng, and X.-L. Zhao, "Joint-sparse-blocks and low-rank representation for hyperspectral unmixing," *IEEE Trans. Geosci. Remote Sens.*, vol. 57, no. 4, pp. 2419–2438, Apr. 2019.

[10] L. Miao and H. Qi, "Endmember extraction from highly mixed data using minimum volume constrained nonnegative matrix factorization," *IEEE Trans. Geosci. Remote Sens.*, vol. 45, no. 3, pp. 765–777, Mar. 2007.

[11] D. M. Rogge, B. Rivard, J. Zhang, and J. Feng, "Iterative spectral unmixing for optimizing per-pixel endmember sets," *IEEE Trans. Geosci. Remote Sens.*, vol. 44, no. 12, pp. 3725–3736, Dec. 2006.

[12] J. W. Boardman, F. A. Kruse, and R. O. Green, "Mapping target signatures via partial unmixing of aviris data," in *Proc. 15th JPL Airborne Earth Sci. workshop Summaries*, 1995, pp. 3–6.

[13] J. C. Harsanyi and C.-I. Chang, "Hyperspectral image classification and dimensionality reduction: An orthogonal subspace projection approach," *IEEE Trans. Geosci. Remote Sens.*, vol. 32, no. 4, pp. 779–785, Jul. 1994.

[14] J. M. Nascimento and J. M. Dias, "Vertex component analysis: A fast algorithm to unmix hyperspectral data," *IEEE Trans. Geosci. Remote Sens.*, vol. 43, no. 4, pp. 898–910, Apr. 2005.

[15] M. E. Winter, "N-findr: An algorithm for fast autonomous spectral endmember determination in hyperspectral data," in *Imaging Spectrometry V*, vol. 3753. Bellingham, WA, USA: International Society for Optics and Photonics, 1999, pp. 266–276.

[16] C.-I. Chang, C.-C. Wu, W. Liu, and Y.-C. Ouyang, "A new growing method for simplex-based endmember extraction algorithm," *IEEE Trans. Geosci. Remote Sens.*, vol. 44, no. 10, pp. 2804–2819, Oct. 2006.

[17] T.-H. Chan, W.-K. Ma, A. Ambikapathi, and C.-Y. Chi, "A simplex volume maximization framework for hyperspectral endmember extraction," *IEEE Trans. Geosci. Remote Sens.*, vol. 49, no. 11, pp. 4177–4193, Nov. 2011.

[18] R. Neville, "Automatic endmember extraction from hyperspectral data for mineral exploration," in *Proc. 4th/21st Canadian Symp. Remote Sens. Int. Airborne Remote Sens. Conf. Exhib.*, 1999, pp. 21–24.

[19] D. C. Heinz and Chein-I-Chang,"Fully constrained least squares linear spectral mixture analysis method for material quantification in hyperspectral imagery," *IEEE Trans. Geosci. Remote Sens.*, vol. 39, no. 3, pp. 529–545, Mar. 2002.

[20] M. D. Craig, "Minimum-volume transforms for remotely sensed data," *IEEE Trans. Geosci. Remote Sens.*, vol. 32, no. 3, pp. 542–552, May 1994.

[21] T.-H. Chan, C.-Y. Chi, Y.-M. Huang, and W.-K. Ma, "A convex analysis-based minimum-volume enclosing simplex algorithm for hyperspectral unmixing," *IEEE Trans. Signal Process.*, vol. 57, no. 11, pp. 4418–4432, Nov. 2009.

[22] J. M. Bioucas-Dias, "A variable splitting augmented Lagrangian approach to linear spectral unmixing," in *Proc. 1st IEEE Workshop Hyperspectral Image Signal Process., Evol. Remote Sens.*, 2009, pp. 1–4.

[23] J. Li, A. Agathos, D. Zaharie, J. M. Bioucas-Dias, A. Plaza, and X. Li, "Minimum volume simplex analysis: A fast algorithm for linear hyperspectral unmixing," *IEEE Trans. Geosci. Remote Sens.*, vol. 53, no. 9, pp. 5067–5082, Sep. 2015.

[24] J. M. P. Nascimento and J. M. Bioucas-Dias, "Hyperspectral unmixing based on mixtures of Dirichlet components," *IEEE Trans. Geosci. Remote Sens.*, vol. 50, no. 3, pp. 863–878, Mar. 2012.

[25] M. Berman, H. Kiiveri, R. Lagerstrom, A. Ernst, R. Dunne, and J. F. Huntington, "ICE: A statistical approach to identifying endmembers in hyperspectral images," *IEEE Trans. Geosci. Remote Sens.*, vol. 42, no. 10, pp. 2085–2095, Oct. 2004.

[26] V. Chandola, A. Banerjee, and V. Kumar, "Anomaly detection: A survey," *ACM Comput. Surv.*, vol. 41, no. 3, 2009, Art. no. 15.

[27] M. Xu, L. Zhang, and B. Du, "An image-based endmember bundle extraction algorithm using both spatial and spectral information," *IEEE J. Sel. Topics Appl. Earth Observ. Remote Sens.*, vol. 8, no. 6, pp. 2607–2617, Jun. 2015.

[28] T. Han, D. G. Goodenough, A. Dyk, and J. Love, "Detection and correction of abnormal pixels in hyperion images," in *Proc. IEEE Int. Geosci. Remote Sens. Symp.*, 2002, vol. 3, pp. 1327–1330.

[29] A. Plaza, P. Martínez, R. Pérez, and J. Plaza, "Spatial/spectral endmember extraction by multidimensional morphological operations," *IEEE Trans. Geosci. Remote Sens.*, vol. 40, no. 9, pp. 2025–2041, Sep. 2002.

[30] D. M. Rogge, B. Rivard, J. Zhang, A. Sanchez, J. Harris, and J. Feng, "Integration of spatial-spectral information for the improved extraction of endmembers," *Remote Sens. Environ.*, vol. 110, no. 3, pp. 287–303, 2007.

[31] H. Li and L. Zhang, "A hybrid automatic endmember extraction algorithm based on a local window," *IEEE Trans. Geosci. Remote Sens.*, vol. 49, no. 11, pp. 4223–4238, Nov. 2011.

[32] S. Mei, M. He, Z. Wang, and D. Feng, "Spatial purity based endmember extraction for spectral mixture analysis," *IEEE Trans. Geosci. Remote Sens.*, vol. 48, no. 9, pp. 3434–3445, Sep. 2010.

[33] X. Shen and W. Bao, "Hyperspectral endmember extraction using spatially weighted simplex strategy," *Remote Sens.*, vol. 11, no. 18, 2019, Art. no. 2147.

[34] M. Zortea and A. Plaza, "Spatial preprocessing for endmember extraction," *IEEE Trans. Geosci. Remote Sens.*, vol. 47, no. 8, pp. 2679–2693, Aug. 2009.

[35] G. Martin and A. Plaza, "Spatial-spectral preprocessing prior to endmember identification and unmixing of remotely sensed hyperspectral data," *IEEE J. Sel. Topics Appl. Earth Observ. Remote Sens.*, vol. 5, no. 2, pp. 380–395, Apr. 2012.

[36] X. Xu, J. Li, C. Wu, and A. Plaza, "Regional clustering-based spatial preprocessing for hyperspectral unmixing," *Remote Sens. Environ.*, vol. 204, pp. 333–346, 2018.

[37] W. R. Tobler, "A computer movie simulating urban growth in the Detroit region," *Econ. Geography*, vol. 46, no. sup1, pp. 234–240, 1970.

[38] Y. Tarabalka, M. Fauvel, J. Chanussot, and J. A. Benediktsson, "SVM-and MRF-based method for accurate classification of hyperspectral images," *IEEE Geosci. Remote Sens. Lett.*, vol. 7, no. 4, pp. 736–740, Oct. 2010.

[39] M. Khodadadzadeh, J. Li, A. Plaza, H. Ghassemian, J. M. Bioucas-Dias, and X. Li, "Spectral-spatial classification of hyperspectral data using local and global probabilities for mixed pixel characterization," *IEEE Trans. Geosci. Remote Sens.*, vol. 52, no. 10, pp. 6298–6314, Oct. 2014.

[40] J. Xia, J. Chanussot, P. Du, and X. He, "Spectral-spatial classification for hyperspectral data using rotation forests with local feature extraction and Markov random fields," *IEEE Trans. Geosci. Remote Sens.*, vol. 53, no. 5, pp. 2532–2546, May 2015.
[41] O. Eches, N. Dobigeon, and J.-Y. Tourneret, "Enhancing hyperspectral image unmixing with spatial correlations," *IEEE Trans. Geosci. Remote Sens.*, vol. 49, no. 11, pp. 4239–4247, Nov. 2011.
[42] W. Li, S. Prasad, and J. E. Fowler, "Hyperspectral image classification using Gaussian mixture models and Markov random fields," *IEEE Geosci. Remote Sens. Lett.*, vol. 11, no. 1, pp. 153–157, Jan. 2014.
[43] J. W. Boardman, "Geometric mixture analysis of imaging spectrometry data," in *Proc. IEEE Int. Geosci. Remote Sens. Symp.*, 1994, vol. 4, pp. 2369–2371.
[44] C.-I. Chang and Q. Du, "Estimation of number of spectrally distinct signal sources in hyperspectral imagery," *IEEE Trans. Geosci. Remote Sens.*, vol. 42, no. 3, pp. 608–619, Mar. 2004.
[45] S. Geman and D. Geman, "Stochastic relaxation, Gibbs distributions, and the Bayesian restoration of images," in *Readings in Computer Vision*. Amsterdam, Netherlands: Elsevier, 1987, pp. 564–584.
[46] R. J. Baxter, *Exactly Solved Models in Statistical Mechanics*. Amsterdam, Netherlands: Elsevier, 2016.
[47] M. O. Smith, P. E. Johnson, and J. B. Adams, "Quantitative determination of mineral types and abundances from reflectance spectra using principal components analysis," *J. Geophysical Res., Solid Earth*, vol. 90, no. S02, pp. C797–C804, 1985.
[48] N. R. Pal, K. Pal, J. M. Keller, and J. C. Bezdek, "A possibilistic fuzzy c-means clustering algorithm," *IEEE Trans. Fuzzy Syst.*, vol. 13, no. 4, pp. 517–530, Aug. 2005.
[49] J. A. Bilmes *et al.*, "A gentle tutorial of the EM algorithm and its application to parameter estimation for Gaussian mixture and hidden Markov models," *Int. Comput. Sci. Inst.*, vol. 4, no. 510, pp. 126–140, 1998.
[50] F. Kowkabi, H. Ghassemian, and A. Keshavarz, "Hybrid preprocessing algorithm for endmember extraction using clustering, over-segmentation, and local entropy criterion," *IEEE J. Sel. Topics Appl. Earth Observ. Remote Sens.*, vol. 10, no. 6, pp. 2940–2949, Jun. 2017.
[51] S. Panda, S. Sahu, P. Jena, and S. Chattopadhyay, "Comparing fuzzy-c means and k-means clustering techniques: A comprehensive study," in *Advances in Computer Science, Engineering & Applications*. New York, NY, USA: Springer, 2012, pp. 451–460.
[52] H. Shah-Hosseini, "SLIC superpixels compared to state-of-the-art superpixel methods," *IEEE Trans. Pattern Anal. Mach. Intell*, vol. 34, no. 11, pp. 2274–2282, 2012.
[53] E. Kaltofen and G. Villard, "On the complexity of computing determinants," *Comput. Complexity*, vol. 13, no. 3-4, pp. 91–130, 2005.
[54] Y. Zhou, A. Rangarajan, and P. D. Gader, "A Gaussian mixture model representation of endmember variability in hyperspectral unmixing," *IEEE Trans. Image Process.*, vol. 27, no. 5, pp. 2242–2256, May 2018.
[55] S. Ozkan and G. B. Akar, "Improved deep spectral convolution network for hyperspectral unmixing with multinomial mixture kernel and endmember uncertainty," 2018, *arXiv:1808.01104*.
[56] D. L. Davies and D. W. Bouldin, "A cluster separation measure," *IEEE Trans. Pattern Anal. Mach. Intell.*, vol. PAMI-1, no. 2, pp. 224–227, Apr. 1979.
[57] M. Xu, B. Du, and L. Zhang, "Spatial-spectral information based abundance-constrained endmember extraction methods," *IEEE J. Sel. Topics Appl. Earth Observ. Remote Sens.*, vol. 7, no. 6, pp. 2004–2015, Jun. 2014.
[58] S. Mei, M. He, Y. Zhang, Z. Wang, and D. Feng, "Improving spatial-spectral endmember extraction in the presence of anomalous ground objects," *IEEE Trans. Geosci. Remote Sens.*, vol. 49, no. 11, pp. 4210–4222, Nov. 2011.
[59] F. Zhu, Y. Wang, S. Xiang, B. Fan, and C. Pan, "Structured sparse method for hyperspectral unmixing," *ISPRS J. Photogrammetry Remote Sens.*, vol. 88, pp. 101–118, 2014.
[60] J. M. Bioucas-Dias and J. M. Nascimento, "Hyperspectral subspace identification," *IEEE Trans. Geosci. Remote Sens.*, vol. 46, no. 8, pp. 2435–2445, Aug. 2008.
[61] F. Zhu, Y. Wang, B. Fan, G. Meng, and C. Pan, "Effective spectral unmixing via robust representation and learning-based sparsity," 2014, *arXiv:1409.0685*.

Xiangfei Shen received the B.S. degree in computer science and technology from North Minzu University, Yinchuan, China, 2017. He is currently working toward the M.S. degree with the School of Computer Science and Engineering, North Minzu University, Yinchuan, China.

His research interests include hyperspectral image processing, pattern recognition, and machine learning.

Wenxing Bao received the B.Eng. degree in industrial automation from Xidian University, Xi'an, China, in 1993, the M.Sc. degree in electrical engineering from Xi'an Jiaotong University, Xi'an, China, in 2001, and the Ph.D. degree in electronic science and technology from Xi'an Jiaotong University, Xi'an, China, in 2006.

He is currently a Professor and Vice President of North Minzu University, Yinchuan, China. His research interests include digital image processing, remote sensing image classification, and fusing.

Kewen Qu received the B.Eng. degree in computer science from Henan University, Kaifeng, China, in 2008, and the M.Sc. degree in computer science from North Minzu University, Yinchuan, China, in 2012. He is currently working toward the Ph.D. degree with the School of Computer and Information, Hefei University of Technology, Hefei, China.

His current research interests include hyperspectral image processing, machine learning, and computer vision.